Epitaxial synthesis of unintentionally doped *p*-type SnO (001) via *suboxide* molecular beam epitaxy

Kingsley Egbo, Esperanza Luna, Jonas Lähnemann, et al.

View Online   Export Citation   CrossMark

ARTICLES YOU MAY BE INTERESTED IN

Formation of a-type dislocations near the InGaN/GaN interface during post-growth processing of epitaxial structures
Journal of Applied Physics **133**, 045304 (2023); https://doi.org/10.1063/5.0128514

Analysis of the ionic and dielectric properties of perovskites by impedance spectroscopy
Journal of Applied Physics **133**, 045501 (2023); https://doi.org/10.1063/5.0123547

Positive temperature coefficient of resistance of Mg-GeO$_2$ nanowire array film
Journal of Applied Physics **133**, 045302 (2023); https://doi.org/10.1063/5.0130729

Epitaxial synthesis of unintentionally doped *p*-type SnO (001) via *suboxide* molecular beam epitaxy

Kingsley Egbo,[1,a)] (ID) Esperanza Luna,[1] (ID) Jonas Lähnemann,[1] (ID) Georg Hoffmann,[1] (ID) Achim Trampert,[1] (ID)
Jona Grümbel,[2] (ID) Elias Kluth,[2] (ID) Martin Feneberg,[2] (ID) Rüdiger Goldhahn,[2] (ID) and Oliver Bierwagen[1,b)] (ID)

AFFILIATIONS

[1]Paul-Drude-Institut für Festkörperelektronik, Leibniz-Institut im Forschungsverbund Berlin e.V., Hausvogteiplatz 5-7,
10117 Berlin, Germany
[2]Institut für Physik, Otto-von-Guericke-Universität Magdeburg, Universitätsplatz 2, 39106 Magdeburg, Germany

[a)]Author to whom correspondence should be addressed: egbo@pdi-berlin.de
[b)]bierwagen@pdi-berlin.de

ABSTRACT

By employing a mixed SnO_2 + Sn source, we demonstrate *suboxide* molecular beam epitaxy (S-MBE) growth of phase-pure single-crystalline metastable SnO (001) thin films on Y-stabilized ZrO_2 (001) substrates at a growth rate of ~1.0 nm/min without the need for additional oxygen. These films grow epitaxially across a wide substrate temperature range from 150 to 450 °C. Hence, we present an alternative pathway to overcome the limitations of high Sn or SnO_2 cell temperatures and narrow growth windows encountered in previous MBE growth of metastable SnO. *In situ* laser reflectometry and line-of-sight quadrupole mass spectrometry were used to investigate the rate of SnO desorption as a function of substrate temperature. While SnO ad-molecule desorption at T_S = 450 °C was growth-rate limiting, the SnO films did not desorb at this temperature after growth in vacuum. The SnO (001) thin films are transparent and unintentionally *p*-type doped, with hole concentrations and mobilities in the range of 0.9–6.0 × 10^{18} cm^{-3} and 2.0–5.5 cm^2 V^{-1} s^{-1}, respectively. These *p*-type SnO films obtained at low substrate temperatures are promising for back-end-of-line (BEOL) compatible applications and for integration with *n*-type oxides in *pn* heterojunctions and field-effect transistors.

I. INTRODUCTION

Tin (II) oxide (SnO) is a valuable *p*-type oxide material useful in several technological applications, such as in *pn* diodes, transistors, solar cells, and solid-state gas sensing.[1,2] It is among the few binary oxide materials that show unintentional *p*-type character due to native defects.[3–7] Though SnO has a low indirect fundamental bandgap of 0.7 eV, an optical bandgap of ~2.7–2.9 eV makes it a suitable component for several transparent applications.[8,9] SnO crystallizes in a layered tetragonal litharge structure with space group P4/nmm, with four oxygen atoms and a Sn atom forming a pyramid structure.[10,11] Due to a more dispersed valence band maximum composed of hybridized Sn 5*s* and the O 2*p* orbitals,[12,13] reasonably high mobilities compared to most *p*-type oxides have been reported for polycrystalline and single-crystalline SnO thin films.[14–16] As most metal oxides show a propensity for *n*-type conductivity and due to the difficulty in their bipolar doping, efforts in

oxide electronics mostly depend on oxide heterojunctions. Hence, SnO has become a major *p*-type oxide for oxide heterojunctions due to its high mobility compared to other *p*-type oxides.[17–21]

Unlike tin (IV) oxide (SnO_2), SnO is metastable, and this presents a growth challenge with competing stable metallic Sn or SnO_2 as well as Sn_3O_4 phases, which may coexist along with SnO phase in the thin films. Though several growth techniques have been employed for the growth of polycrystalline SnO,[20] phase-pure single crystal SnO layers have been mostly obtained by electron beam evaporation,[22] pulsed laser deposition,[8] and molecular beam epitaxy. High-quality single-crystalline SnO has been grown by plasma-assisted MBE (PA-MBE) using a metal Sn source[23] and S-MBE using an oxide SnO_2 source.[24] However, both methods present challenges; the plasma-assisted growth of SnO using a Sn metal source requires the Sn effusion cell to be operated at very high temperatures up to 1175 °C and the growth window is limited

by the formation of SnO_2 and oxygen rich Sn compounds, such as Sn_3O_4, requiring a rigorous fine tuning of a Sn/O flux ratio.[23] Also, growth using an oxide SnO_2 charge involves high temperature decomposition of the oxide into the SnO suboxide and a parasitic oxygen background ($2\,SnO_2 \rightarrow 2\,SnO + O_2$). Previously, it has been proposed that the sublimation of a mixed oxide + metal charge in an effusion cell can provide an effective suboxide flux for the growth of oxides by MBE.[25] For instance, some of us have shown that a reaction of mixed $SnO_2 + Sn$ metal charge to give SnO ($SnO_2 + Sn \rightarrow 2\,SnO$) as well as a non-negligible fraction of Sn_2O_2, can be an efficient source of SnO flux, for suboxide-MBE growth of SnO_2.[25] This suboxide approach offers the advantages that the reaction in the source takes place at lower effusion-cell temperatures, free of parasitic oxygen formation, and growth of SnO can proceed without the need to provide additional oxygen. It remains to be clarified, however, if the fraction of Sn_2O_2 in the suboxide flux, not present when using pure SnO_2 source material, is detrimental for the SnO growth.

Following this *suboxide*-MBE (S-MBE) approach using a mixed source, we present in this study the growth of SnO thin films without the need for plasma-activated oxygen or intentional background oxygen. SnO is grown heteroepitaxially on Y-stabilized ZrO_2 [YSZ (001)] and r-plane Al_2O_3 in a substrate temperature, T_S window from 50 to 650 °C. We investigate the impact of T_S on the phase purity, growth-rate-limiting SnO desorption as well as structural and transport properties of the SnO layers. A schematic comparison of the conventional method of PA-MBE using a metal source and the S-MBE approach employed in this work is described in Figs. 1(a) and 1(b), respectively. Detailed investigation of the growth kinetics for our SnO growth using this S-MBE approach indicates that the growth rate is limited by the desorption of the

adsorbed SnO molecules, which increase with the substrate temperature; however, grown single SnO crystalline layers are stable and show negligible desorption at substrate temperatures $\leq$450 °C. We show that while amorphous layers were obtained at $T_S = 50$ °C, textured and single-crystalline phase-pure unintentionally (UID) doped p-type SnO(001) films are grown between substrate temperatures of 150 and 450 °C. Above 550 °C, secondary Sn_3O_4 and Sn phases are present in the SnO layer. Obtained single-crystalline SnO(001) layers at low T_S between 150 and 250 °C show good UID transport properties. It is well known that epitaxial and single-crystalline channel layers result in superior qualities in devices such as thin film transistors; however, epitaxial deposition of active layers usually requires high substrate temperatures that exceed the BEOL limit. Hence, these epitaxially grown SnO thin films obtained for T_S between 150 and 250 °C can be promising for applications as active layers for BEOL compatible device development.

II. EXPERIMENTAL

Approximately 100–190 nm-thick UID SnO(001) thin films were deposited in an MBE chamber with solid-source effusion cells. While most growth were performed on YSZ (001), r-plane Al_2O_3 substrates were also co-loaded for several growth runs. To grow SnO, a $SnO_2 + Sn$ mixed source was sublimed from an effusion cell with an Al_2O_3 crucible at temperatures between 740 and 820 °C. The hot-lip of the used dual-filament cell was kept at 150 °C above the $SnO_2 + Sn$-cell temperature. The resulting source beam equivalent pressure (BEP), proportional to the particle flux and measured using a nude filament ion gauge positioned at the substrate location, is about 0.4–1.5×10^{-7} mbar for all growth runs. Before growth, the substrates, with $1\,\mu m$ thick Ti sputter-deposited on the backside to improve substrate radiative heating, were oxygen-plasma treated in the growth chamber for 30 min at substrate temperatures, T_S between 400 and 700 °C using 1 standard cubic centimeters per minute (SCCM) O_2 and 200 W plasma power. The T_S monitored *in situ* by a thermocouple between the substrate and heating filament was varied between 50 and 650 °C for different growth runs. The background pressure of the chamber during SnO deposition was $P_{GC} \sim 5$–8×10^{-8} mbar without plasma-activated oxygen and any intentional molecular oxygen. The growth rate and the amount of desorbing flux were measured *in situ* by laser reflectometry (LR) and line-of-sight quadrupole mass spectrometry (QMS).[26]

Different *ex situ* techniques were used to characterize the grown SnO layers. A four-circle x-ray lab-diffractometer (X'pert Pro MRD from Philips PANalytical) equipped with a Cu Kα radiation source was used to investigate the crystallographic orientation of the film and the epitaxial relationship with the substrate. The out-of-plane orientation was analyzed by means of symmetric on-axis 2Θ-ω scans with a 1 mm detector slit. The in-plane epitaxial relationship between the SnO film and the YSZ substrates was measured by Φ-scans in a skew-symmetric geometry. On-axis rocking curve ω-scans were used to investigate the crystalline quality of the films and texture maps in a skew-symmetric geometry were used to validate the phase purity. Bulk-sensitive room-temperature Raman spectroscopy measurements in the backscattering geometry using a solid-state laser at a wavelength of 473 nm were used to investigate
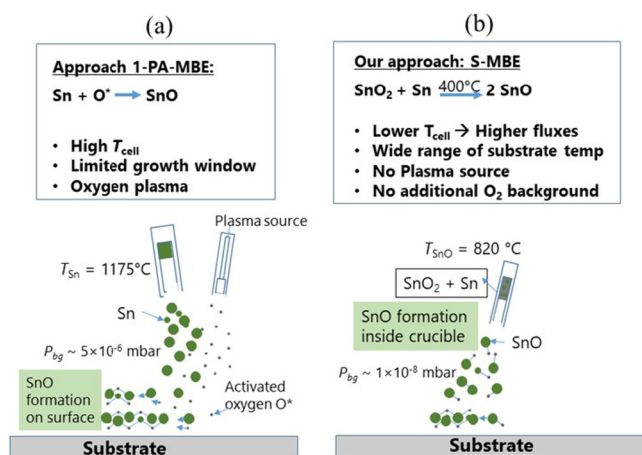

FIG. 1. (a) Schematic of the formation of SnO layers on a substrate using the PA-MBE approach with Sn charge and (b) S-MBE approach using mixed $SnO_2 + Sn$ charge. In the PA-MBE approach, a Sn metal cell operated at a very high cell temperature supplies Sn metal fluxes, and a plasma source provides activated oxygen leading to the formation of SnO on the film surface, while in the S-MBE approach, SnO is formed in the crucible by the mixture and films are deposited in a high vacuum without activated or molecular oxygen present.

the grown layers as described in Ref. 23. Surface morphology of the grown layers was analyzed by atomic force microscopy (AFM) using a Bruker Dimension Edge in the peak force tapping mode. (Scanning) transmission electron microscopy [(S)TEM] was used to study the film's microstructure. TEM observations were made with a JEOL 2100F microscope operating at 200 kV. Cross-sectional TEM specimens were prepared for observation in both $\langle 011 \rangle$ projections of the YSZ substrate using standard mechanical polishing and dimpling, followed by argon ion-milling, starting at 3.0 keV and finishing at 1.5 keV. The film domain structures and orientation were further investigated by top-view electron backscatter diffraction (EBSD) measurements in a scanning electron microscope operated at 15 kV. Hall measurements in the van der Pauw geometry were used to investigate the transport properties of the layers grown at different substrate temperatures. Because of the low mobilities obtained for some of the grown layers, a magnetic sweep method was used to extract reliable Hall coefficients.[27] To compare the optical properties of grown layers with existing literature,[24] spectroscopic ellipsometry measurement and modeling were performed on a layer grown on r-plane Al_2O_3 at a substrate temperature of 400 °C.

III. RESULTS AND DISCUSSIONS

A. Thermodynamics of the suboxide source and SnO growth window

Previously from a quadrupole mass spectrometry study, we have demonstrated that a reaction of a mixed oxide + metal charge can serve as an efficient source of suboxides such as Ga_2O and

SnO.[25] By taking advantage of this suboxide source, we determine the growth window and thermodynamic consideration for the growth of metastable p-type SnO from a $SnO_2 + Sn$ mixture.[23,28] Figure 2(a) shows the calculated SnO_2–Sn equilibrium phase diagram as a function of stoichiometry, $n_{Sn}/(n_{Sn} + n_{SnO2})$ and temperature calculated at 10^{-7} mbar typical for MBE growth without O_2 environment. This thermodynamic equilibrium diagram calculated using FactSage[29] indicates that stable SnO in the solid phase can be obtained at growth temperatures within 190–420 °C at a stoichiometry of $n_{Sn}/(n_{Sn} + n_{SnO2}) = 0.5$. Here, ideal gas indicates gaseous species of the constituent elements in the reaction.[25] This supports our experimental data where phase-pure SnO was obtained between 150 and 450 °C substrate temperatures during growth as discussed below. Due to the absence of reactive oxygen during growth, we can obtain phase-pure SnO for Sn stoichiometry of 0.5 in $n_{Sn}/(n_{Sn} + n_{SnO2})$, which was used throughout this growth experiment. Figure 2(b) shows the corresponding phase diagrams for the mixed charges at Sn stoichiometry, $n_{Sn}/(n_{Sn} + n_{SnO2}) = 0.5$ indicating the vapor pressure of suboxide SnO as a function of source temperatures for the mixed charges. These mixed sources promote the availability of required suboxide vapor pressure at lower source temperatures compared to the metal charge and solid oxide charge.[25]

B. SnO flux, rate of desorption, and disproportionation of the layer

In the identified growth window for SnO suboxide growth, the growth rate is given by the difference in the amount of arriving SnO species (proportional to the vapor pressure of the SnO
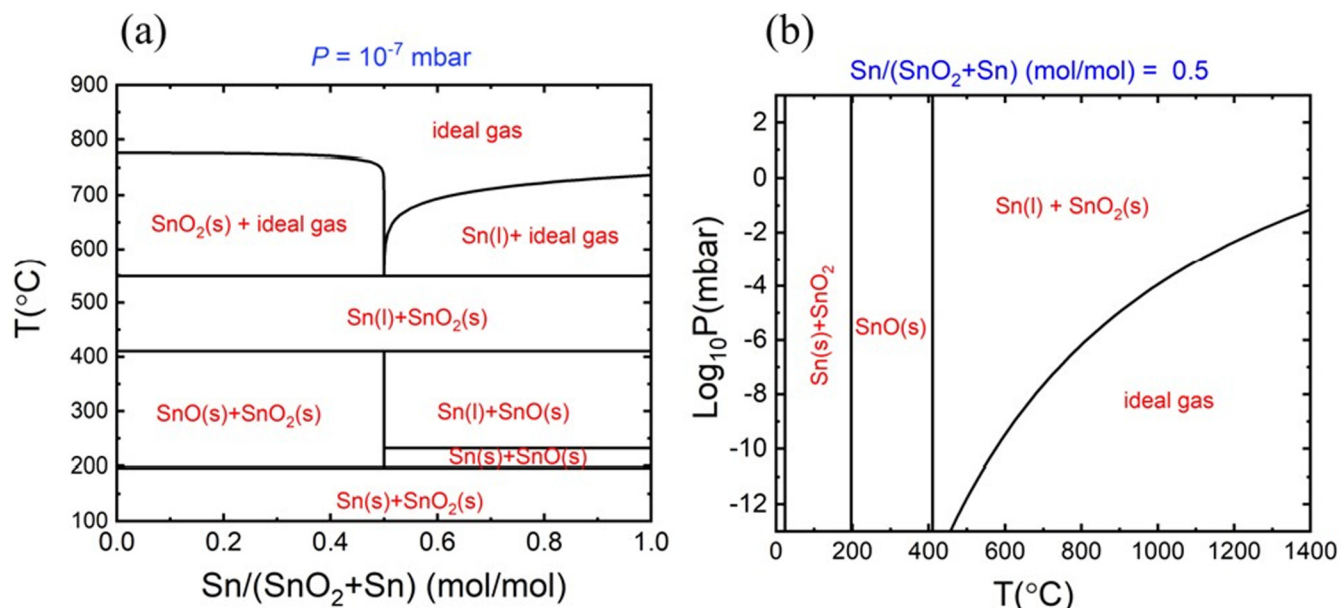

FIG. 2. (a) Equilibrium phase diagram of the SnO_2–Sn system as a function of stoichiometry and temperature at a pressure of 10^{-7} mbar typical for MBE growth without intentional oxygen background. Stoichiometries of $n_{Sn}/(n_{Sn} + n_{SnO2}) = 0$, 0.5 and 1 correspond to SnO_2; SnO and pure Sn, respectively. (b) Phase diagram of the SnO_2–Sn system for $n_{Sn}/(n_{Sn} + n_{SnO2}) = 0.5$ as a function of temperature and pressure.

[cf. Figure 2(b)] at the cell temperature of the mixed source) and the amount of desorbing species (which increases with increasing substrate temperature). This promotes a simpler growth kinetics compared to SnO growth by PA-MBE in which rigorous Sn/O flux calibration is required to limit the formation of competing O-rich and Sn-rich phases. The SnO flux impinging on a substrate from the mixed $SnO_2 + Sn$ effusion cell is equivalent to the measured BEP in the absence of an oxygen background. In order to characterize the kinetics of the mixed $SnO_2 + Sn$ effusion cell, we measured the BEP as a function of source temperature from 740 to 800 °C in the absence of any active O_2 flow (see Fig. 3). The curve shows the expected exponential dependence with an activation energy for SnO of 2.4 eV, similar to the value obtained by our previous QMS results.[25] The incorporated cation flux on the substrate (solid symbols in Fig. 3, obtained as the product of the measured growth rate and the cation density) is proportional to the BEP as expected for full cation incorporation due to the low growth temperature of 50 °C, i.e., without desorption from the substrate.

Using line-of-sight quadrupole mass spectrometry, we identify the rate of desorption of the SnO ad-molecules during growth as a function of substrate temperature. Our measurement reveals that the desorbing flux significantly decreases with decreasing substrate temperature as shown in Fig. 4(a). The inset of Fig. 4(a) shows a typical QMS spectrum recorded during SnO desorption at high substrate temperatures. For a flux of 4×10^{13} cm^{-2} s^{-1} reaching the substrate with a substrate temperature of 450 °C, a growth rate of 1.0 nm/min is expected; however, a SnO growth rate of ~0.6 nm/min is obtained from the LR oscillation in Fig. S1 in the supplementary material; hence, the desorption rate of the SnO

ad-molecules is ~0.3 nm/min (1.4×10^{13} cm^{-2} s^{-1}). From the plot of desorption rate as a function of substrate temperature, an activation energy of desorption of ~0.3 eV is obtained, and this low activation energy value indicates a high volatility of the suboxide ad-molecules during growth. The desorption rate at higher substrate temperatures is limited by the amount of flux reaching the substrate as seen in Fig. 4(a). While these ad-molecules are volatile during growth, to further understand the stability of the SnO molecules within the film after growth, we perform a separate LR study at a SnO film grown at a BEP of 1.3×10^{-7} mbar. From Fig. 3, this BEP corresponds to a flux at the substrate of 8.6×10^{13} cm^{-2} s^{-1} (assuming full incorporation) and to a growth rate of 1.85 nm/min. However, Fig. 4(b) shows only a growth rate of 1.2 nm/min obtained from the oscillatory half period t_{growth} of the laser reflectometry signal[26] for growth at 450 °C substrate temperature, which is the highest temperature where phase-pure SnO is obtained. Hence, the SnO ad-molecules have a desorption rate of ~0.65 nm/min during growth corresponding to a desorbing flux of 3.0×10^{13} cm^{-2} s^{-1}. When the SnO shutter is closed, and the substrate temperature maintained at 450 °C the reflected laser signal is constant indicating negligible desorption of stabilized SnO species on the substrate. This is in contrast to the high desorbing flux of 3.0×10^{13} cm^{-2} s^{-1} for the SnO ad-molecules during growth at 450 °C, indicating that once the SnO molecule stabilizes in a layer, its activation energy for desorption is higher than for directly re-evaporated SnO ad-molecules. Finally, with an increase in the substrate temperature to 550 °C, an onset of an oscillation is observed due to SnO desorption or increasing roughness due to the disproportionation of the grown layer. Note that this reflected signal oscillation has a weak amplitude compared to the growth oscillation pointing to the roughening of the layer and formation of other Sn-compound phases. Therefore, while SnO ad-molecules desorb during growth as indicated in Fig. 4(a), SnO layers formed are very stable with negligible desorption rate at the growth temperature.
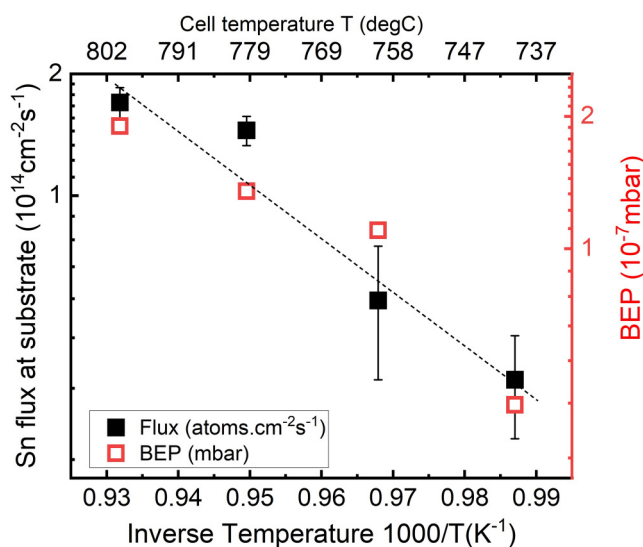
C. Structural properties and epitaxial relation

Wide-angle symmetric 2Θ-ω XRD scans were used to investigate the out-of-plane orientation of the layers. Figure 5(a) shows representative results for layers grown at different YSZ (001) substrate temperatures, wide-angle scans of selected samples between 10 and 120° are shown in Fig. S2(a) in the supplementary material, and similar wide-angle scans for a sample grown on r-plane Al_2O_3 are shown in Fig. S2(b) in the supplementary material. Typical streaky RHEED patterns observed during the growth of SnO (001) layers are also shown in Fig. S3 in the supplementary material. The layer grown at a substrate temperature of 50 °C was amorphous; hence, only substrate peaks are observed in the XRD scan. For layers grown between 150 and 450 °C, only the SnO (001) and higher order reflexes as well as the YSZ (100) substrate peaks are present, indicating phase-pure (001) oriented single-crystalline SnO films. This is in contrast with previous results on plasma-assisted MBE growth of SnO in which phase-pure SnO was only possible at a substrate temperature between 350 and 400 °C.[23] A very limited substrate temperature window was observed in previous S-MBE SnO growth on r-plane Al_2O_3 (1–102) substrates using an SnO_2

FIG. 3. Arrhenius diagram of the incorporated Sn flux (solid symbols) during MBE growth and the corresponding measured BEPs of the mixed $SnO_2 + Sn$ effusion cell (right axis, open symbols). An incorporated flux at the substrate of 4.8×10^{13} cm^{-2} s^{-1} corresponds to a SnO growth rate of 1.0 nm/min and to a BEP of ~7×10^{-8} mbar.
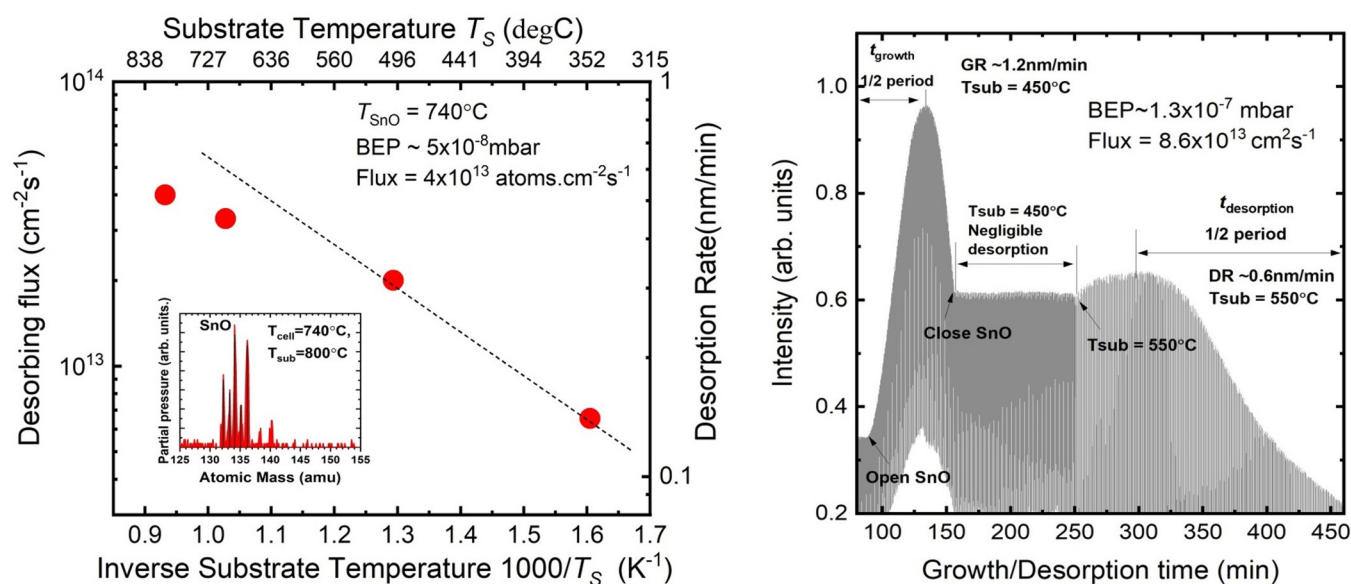
FIG. 4. (a) Arrhenius diagram of the desorbing flux as a function of the substrate temperature. The desorbing species were obtained from the line-of-sight QMS. Their flux increases with increasing substrate temperatures and is limited at high temperatures by the provided SnO flux to the substrates. (b) Plot of the laser reflectometry signal (with substrate rotation causing the high-frequency oscillation artifact) from the film surface during growth and thermal etching at higher substrate temperatures. The opening and closing of the SnO_2 + Sn-cell shutter as well as substrate temperatures are indicated.

source: Mei *et al.* reported that their films grown below 370 °C were amorphous while no deposition occurred above 400 °C.[24] Furthermore, we observe slightly sharper peaks in the 2Θ-ω scans of the samples grown at 250–450 °C, indicating higher crystal quality than that of layers grown at a lower temperature. However, the increase is not linear with increasing substrate temperatures. Once the substrate temperature is increased even further, to 550 °C, the presence of Sn_3O_4 secondary phase and Sn peaks are observed
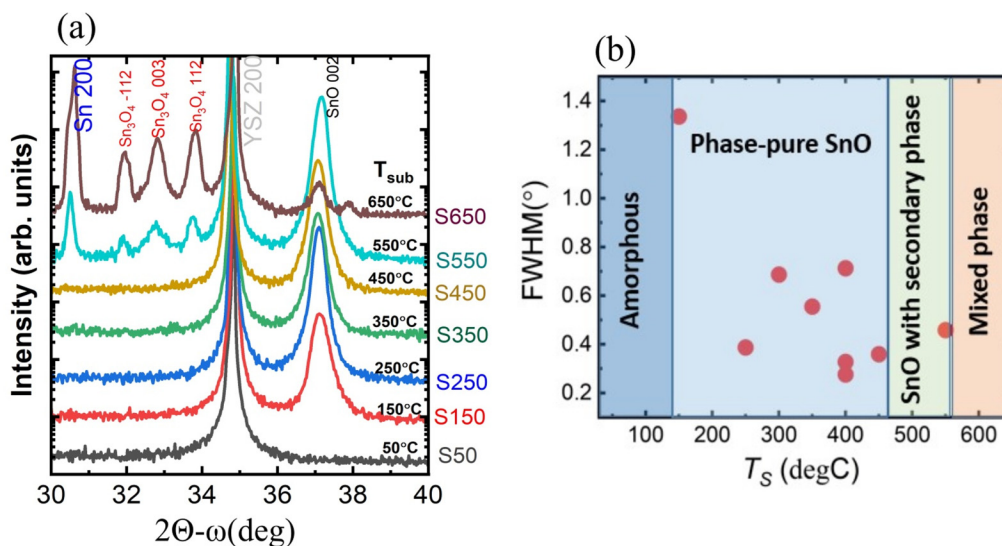

FIG. 5. (a) XRD out-of-plane symmetric 2Θ-ω scan of SnO(001) layer on YSZ(100) grown at different substrate temperatures. The film grown at 50 °C was amorphous, between 150 and 450 °C, phase-pure single-crystalline SnO(001) layers are obtained. At a substrate temperature of 550 °C, secondary Sn_3O_4 phases are observed and growth at 650 °C showed a mixed phase with negligible SnO(001) contribution. (b) FWHM of the SnO 002 omega rocking curve as a function of the substrate temperature.

indicating a disproportionation of the phase-pure SnO to Sn-rich and O-rich phases. This trend is continued with a further increase in a substrate temperature up to 650 °C, where the intensity of a mixed phase (metallic Sn, Sn_3O_4) dominates the XRD and the SnO peak intensity becomes negligible. Figure 5(b) shows the FWHM of the SnO (002) omega rocking curves as a function of a substrate temperature for the grown layers. The FWHM maximum ranges from a high value of 1.3° for the sample grown at a low substrate temperature of 150 °C to values between 0.2 and 0.7° for samples grown at higher substrate temperatures. Film roughness between 2 and 15 nm [root mean square (rms)] is obtained from AFM measurements for the single-crystalline SnO (001) layers.

The in-plane epitaxial relationship between the SnO (001) layer and the substrate was investigated for the phase-pure SnO (001) thin films by skew-symmetric Φ-scans of the SnO 112 and YSZ 111 reflections with rotational angle Φ around the surface normal (see Fig. S4 in the supplementary material). From Fig. 5(a), we confirm the epitaxial relationship SnO(001)||YSZ(001) and SnO (110)||YSZ(010) for the out-of-plane and in-plane directions, respectively, indicating a 45° in-plane rotation of the SnO crystal lattice with respect to the YSZ one. This is in agreement with our previously grown PA-MBE thin films, where the same epitaxial relations are observed.[23] To further verify the in-plane crystalline texture of the grown layers, Fig. 6 shows the texture map of the SnO 101 reflex. The texture map confirms the presence of a predominantly single domain as observed in the Φ-scans. The scan shows four distinct peaks at a tilt angle of Ψ = 51.63° corresponding to the tilt of the (101) plane with respect to the (001) planes. Other Streaky peaks not labeled observed in the texture map are due to the substrate holder as shown in Fig. S5 in the supplementary material. Texture maps also show that distinct in-plane epitaxial relationships are possible for these samples on YSZ(001) substrates

unlike randomly oriented samples observed for growths on Ga_2O_3 substrates.[17,18]

To clarify the phase composition of the grown epilayers beyond the limited capabilities of our out-of-plane XRD scans, room-temperature bulk-sensitive Raman spectroscopy measurements are conducted on the grown layers. Following the peak assignment of Eifert *et al.* (and references therein) and our previously reported study on PA-MBE of SnO, the measured Raman spectra of all S-MBE grown SnO films were compared to phonon modes due to Sn, SnO, and Sn_3O_4[23,30,31] as shown in Fig. 7. Raman spectra of the single-crystalline samples grown between 150 and 450 °C show only SnO B_{1g} (113 cm^{-1}) and A_{1g} (211 cm^{-1}) peaks strongly suggesting that no secondary phases are present. In agreement with the x-ray diffraction data, bulk-sensitive Raman scattering of the sample grown at 550 °C indicates a weak contribution of the Sn_3O_4 phase coexisting with the SnO phase, while the sample grown at 650 °C showed predominantly Sn_3O_4 peaks with weak contributions from Sn and SnO. These samples at 550 °C also show a slight shift in their SnO peak positions likely due to the presence of these secondary phases.

Transmission electron microscopy (TEM) of the sample cross section is used to investigate the microstructure of the SnO layer grown at 400 °C, its interface to the YSZ substrate, and the epitaxial relationship between the YSZ substrates and the SnO layers. The overview bright field image of the SnO films as shown in Fig. 8(a) reveals a layer composed of coalesced grains (their average diameter is about 150 nm), a morphology that suggests a 3-D Volmer-Weber growth mode of SnO on YSZ. The streak RHEED patterns obtained during growth shown Fig. S3 in the supplementary material is, hence, likely due to reflections
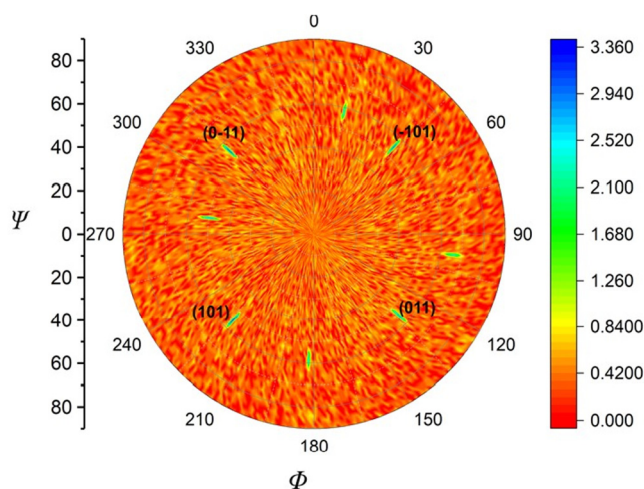

FIG. 6. Texture scan along the (101) peak of SnO. Four peaks obtained for Φ: 0°–360° and Ψ: 0°–90°. Peaks due to the (101) reflex are separated by 90° as expected for the Wulff plot in Fig. S7 in the supplementary material.
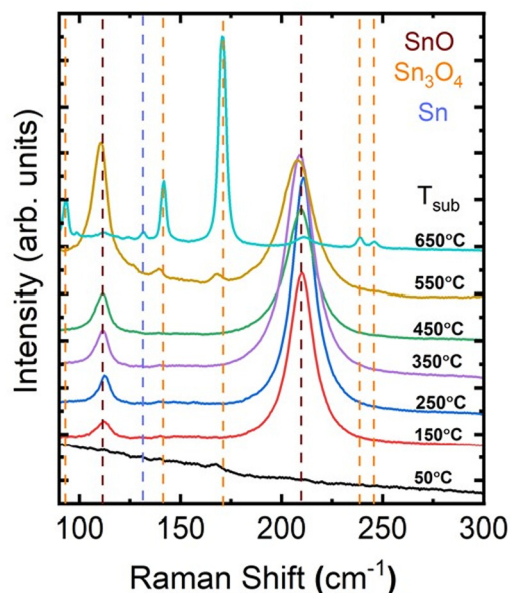

FIG. 7. Bulk-sensitive Raman spectra measured with an excitation wavelength of 473 nm. Vertical lines indicate the peak positions of dominant Raman active phonon modes, in SnO B_{1g} (113) and A_{1g} (211) and in Sn_3O_4, A_g and B_g as indicated by the color code.
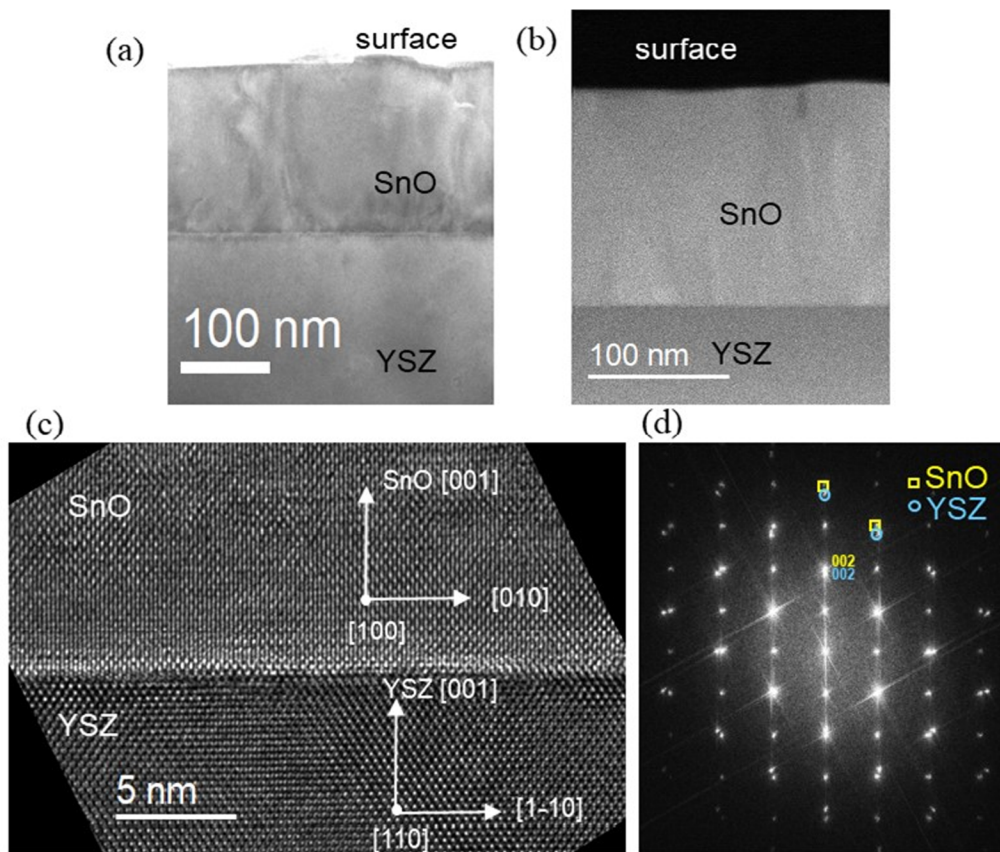
FIG. 8. (a) Cross-sectional TEM image of the SnO(001) film grown at 450 °C (b) High-angle annular dark-field (HAADF) STEM Z-contrast image of the SnO(001)/YSZ(001) hetero-structure. (c) and (d) High-resolution transmission electron microscopy (HRTEM) images of the SnO(001) epilayer on YSZ(001) near the SnO/YSZ interface acquired along the [011] zone axis of YSZ(100). Indexed reflections indicate an $(001)_{SnO} \parallel (001)_{YSZ}$ and $[010]_{SnO} \parallel [1-10]_{YSZ}$ epitaxial relationship as shown in (e) the FFT of the SnO/YSZ micrograph.
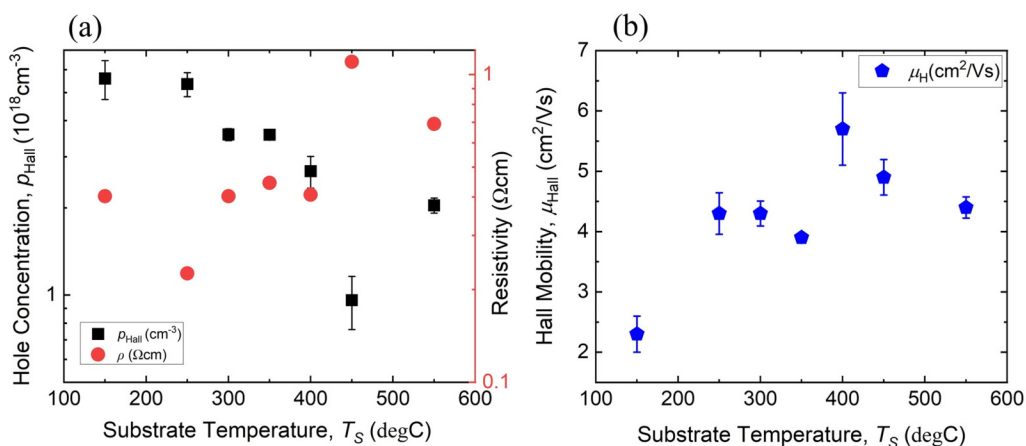

FIG. 9. (a) Hole concentration, p, and resistivity of phase-pure SnO (001) as a function of substrate temperature obtained from Hall measurements in the *van der Pauw* geometry. (b) Hall mobilities of deposited thin films as a function of substrate temperature. The uncertainties for the hole concentration and mobility as shown by error bars are approximately 2%–20%.

TABLE I. Comparison of electrical properties of epitaxial SnO(001) thin films grown using different techniques (S-MBE—suboxide MBE, PA-MBE—plasma-assisted MBE, PLD—pulsed laser deposition, EBE—electron beam evaporation).

Material	Method	T_S (°C)	Growth P_{O_2} (Torr)	Substrate	ω-FWHM (deg)	p_{Hall} (cm^{-3})	Hole mobility (cm^2/V s)	Resistivity (Ω cm)	Reference
SnO (001)	S-MBE	380	5×10^{-7}	r-Al$_2$O$_3$	0.007	2.5×10^{16}	2.4	101	24
SnO (001)	PLD	575	1×10^{-6}	YSZ (001)	0.46	2.5×10^{17}	2.4	…	8
SnO (001)	PLD	200	6×10^{-2}	YSZ (001)	1.0	1.0×10^{17}	2.3	…	35
SnO (001)	EBE	600	…	r-Al$_2$O$_3$	2.9	5.6×10^{17}	0.1	110	9
SnO (001)	EBE	600	$\sim 1 \times 10^{-6}$	r-Al$_2$O$_3$		…	…	195	22
SnO (001)	PA-MBE	350–400	$\sim 5 \times 10^{-6}$	YSZ (001), c-Al$_2$O$_3$	0.4–1.9	1.8–9.7×10^{18}	1–6	0.25–2.0	23
SnO (001)	S-MBE	150–450	$\sim 6 \times 10^{-8}$	YSZ (100)	0.2–1.3	0.9–6×10^{18}	2.5–5.5	0.3–1.2	This Work
SnO (001)	S-MBE	400	$\sim 6 \times 10^{-8}$	r-Al$_2$O$_3$	1.3	7.0×10^{17}	1.4	7.2	This Work

from the surface of these large grains and does not imply a layer-by-layer growth mode. The grains have a single orientation and a well-defined epitaxial relationship. Figure 8(b) displays a high-angle annular dark-field (HAADF) STEM image of the SnO(001)/YSZ(001) heterostructure with atomic number Z-contrast. In this image, SnO shows a brighter contrast compared to YSZ due to its higher average Z. Figure 8(c) displays high-resolution TEM (HRTEM) phase-contrast micrographs of the SnO/YSZ(001) interface acquired along the [011] zone axis of the substrate. Though HRTEM reveals the local presence of steps at the SnO/YSZ interface, there is no noticeable misalignment of the SnO(001) layer, which grows epitaxially on YSZ(001) following the epitaxial relationship (001)$_{SnO}$ ∥ (001)$_{YSZ}$ and [010]$_{SnO}$ ∥ [1–10]$_{YSZ}$. The perfect epitaxial alignment is reflected in the Fast Fourier Transform (FFT) pattern of the image in Fig. 8(d). The epitaxial relationship and crystallographic directions have been determined after a comparison of the experimental data with simulated diffraction patterns obtained using the JEMS simulation program.[32]

Electron backscattering diffraction (EBSD) measured plan-view in a scanning electron microscope was further used to investigate the surface microstructure of our grown layers as the probing depth of EBSD is limited to ~20 nm. Figure S6(a) in the supplementary material shows EBSD mapping of the SnO(001) indicating uniformity of the crystal orientation without any crystal twins on the layer. Figure S7(b) in the supplementary material shows Kikuchi patterns from EBSD measurement and wireframe representation of the indexed orientations.

D. Electrical properties of S-MBE grown UID SnO(001) thin films

The charge carrier transport properties of the UID SnO (001) thin films were obtained at room temperature by Hall measurements in the *van der Pauw* geometry. For the van der Pauw measurement, indium contacts are made on the corners of the as grown UID SnO thin films prior to the measurement.[33] Due to low hole mobilities observed in most *p*-type oxides, extracting accurate Hall voltage using a single magnetic field value B may become ambiguous. Here, to extract reliable Hall coefficients, a Hall sweep between +0.8 and −0.8 T was carried out and the Hall coefficient is obtained from the slope of the Hall voltage as shown in Fig. S7 in the supplementary material. Varying room-temperature UID hole densities, p_{Hall} in the range of 0.9–6.5×10^{18} cm^{-3} are obtained for the phase-pure SnO thin films (S150–S450) as shown in Fig. 9(a). The sample grown at a low substrate temperature of 150 °C shows a remarkable mobility of 2.2 cm^2/V s, increasing the substrate temperatures resulted in the growth of samples with average mobility of 4.5 cm^2/V s as seen in Fig. 9(b). Room-temperature electrical resistivities ρ between 0.3 and 1.2 Ω cm are obtained for the deposited films. A slight spread in transport properties for single-crystalline SnO (001) grown at different temperatures may be related to the growth temperature and crystallinity of the layers, but a consistent trend is not observed. Obtained hole densities in our grown layers are about two orders of magnitude higher than the value reported for UID SnO grown by S-MBE from an SnO$_2$ source.[24] Table I summarizes the room-temperature electrical properties for various reported single-crystalline *p*-type SnO(001) thin films grown using different techniques. The hole densities from these S-MBE grown layers are also slightly lower than our previously reported values grown via PA-MBE. This is likely due to the enhanced formation of Sn vacancies due to the energetics of the different growth process. For S-MBE growth, the SnO flux is reaching the substrate, this is expected to decrease the formation of Sn vacancies and complexes compared to the PA-MBE growth, where elemental Sn and
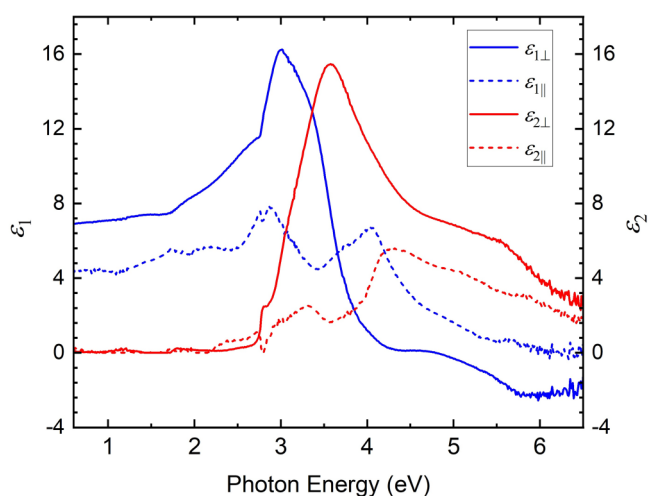
FIG. 10. Complex dielectric function of a SnO(001) thin film resolved into the ordinary *xy* (solid lines) and extraordinary *z* (dashed lines) components obtained from ellipsometry point-by-point fitting.

activated oxygen is supplied. Nevertheless, we cannot rule out unintentionally incorporated extrinsic dopants. To further control the hole concentration of these SnO(001) thin films grown by suboxide MBE, intentional extrinsic doping using Ga and La dopants has been explored, transport measurements for these doped samples show that Ga are efficient acceptor dopants while La acts as compensating donors.[34] S550 films with dominant SnO also showed *p*-type UID properties like the phase-pure SnO layers. Amorphous layers grown at 50 °C were semi-insulating while the mixed phase layer grown at 650 °C showed a *n*-type character.

To assess the optical properties of SnO layers grown via this S-MBE route, spectroscopic ellipsometry measurement and modeling is performed on ~120 nm-thick phase-pure SnO(001) sample grown on r-plane Al_2O_3 at 400 °C. Figure S2(b) in the supplementary material shows the wide-angle 2Θ-ω scan of the sample. Compared to the sample grown on YSZ (001) at a similar substrate temperature, Hall measurements for this sample show a slightly lower hole density and mobility of ~7.0×10^{17} cm^{-3} and ~1.4 cm^2/V s, respectively, and higher resistivity of ~7.2 Ω cm. This decrease in the transport properties is likely due to an increase in strain-induced dislocation density caused by higher lattice mismatch of ~12% in SnO/r-plane Al_2O_3 hetero-interface compared to SnO/YSZ hetero-interface with ~5% lattice mismatch.[23,24] Ordinary and extraordinary complex dielectric function ($\varepsilon \equiv \varepsilon_1 + i\varepsilon_2$) spectra of this thin film extracted from room-temperature spectroscopic ellipsometry measurement are shown in Fig. 10. The ε_2 spectrum in the ordinary direction shows an onset of absorption at ~2.7 eV similar to previously reported values.[24]

IV. CONCLUSIONS

Using an intentional suboxide source comprising a mixed SnO_2 + Sn charge, we demonstrate the heteroepitaxial growth of phase-pure, single-crystalline SnO (001) thin films on YSZ(001)

and r-Al_2O_3 substrates. This S-MBE approach enabled the growth of phase-pure SnO (001) films across a wider growth window and substrate temperatures without plasma-activated oxygen or (un) intentional molecular oxygen. Hence, overcoming the limitation of the narrow growth window previously reported for PA-MBE growth of SnO using a metal charge and S-MBE growth of SnO using a SnO_2 source. We systematically characterized the S-MBE growth kinetics, such as the growth rate and desorbing SnO fluxes as a function of cell temperature, being an important step to employing this suboxide approach to other material systems. *Ex situ* XRD and Raman measurements showed that phase-pure single-crystalline SnO is obtained for a wide substrate temperature window between 150 and 450 °C. Transport and optical measurements also confirm the *p*-type properties and optical transparency of these layers. Hence, with the S-MBE approach, single-crystalline phase-pure SnO(001) was achieved at the lowest substrate temperature of 150 °C so far. This possibility to achieve epitaxial single-crystalline *p*-type SnO (001) thin films for our S-MBE grown samples at low growth temperatures between 150 and 250 °C can promote the integration of these *p*-type SnO layers for BEOL compatible device applications.

SUPPLEMENTARY MATERIAL

See the supplementary material for a typical RHEED image of SnO layers acquired during growth. Wide-angle 2Θ-ω scans of SnO (001) on YSZ(001) and r-Al_2O_3. Skew-symmetric Φ-scans of SnO layer and YSZ substrate, EBSD mapping, and Hall magnetic field sweep data.

ACKNOWLEDGMENTS

AUTHOR DECLARATIONS

Conflict of Interests

The authors have no conflicts to declare.

Author Contributions

Kingsley Egbo: Conceptualization (equal); Data curation (lead); Formal analysis (lead); Investigation (lead); Methodology (lead); Writing – original draft (lead); Writing – review & editing (lead). **Esperanza Luna:** Data curation (supporting); Formal analysis (supporting); Investigation (supporting); Methodology (supporting); Writing – original draft (supporting). **Jonas Lähnemann:** Formal analysis (supporting); Investigation (supporting); Writing – review & editing (supporting). **Georg Hoffmann:** Conceptualization (supporting); Methodology (supporting). **Achim Trampert:** Formal analysis (supporting); Investigation (supporting); Writing – review & editing (supporting). **Jona Grümbel:** Data curation (supporting); Formal analysis (supporting); Investigation (supporting); Writing – original draft (supporting). **Elias Kluth:** Data curation

(supporting); Investigation (supporting). **Martin Feneberg:** Formal analysis (supporting); Investigation (supporting). **Rüdiger Goldhahn:** Formal analysis (supporting); Investigation (supporting). **Oliver Bierwagen:** Conceptualization (equal); Data curation (supporting); Formal analysis (supporting); Investigation (supporting); Project administration (lead); Resources (lead); Writing – review & editing (supporting).

DATA AVAILABILITY

The data that support the findings of this study are available within the article and its supplementary material.

REFERENCES

[1] Z. Wang, P. K. Nayak, J. A. Caraveo-Frescas, and H. N. Alshareef, Adv. Mater. **28**, 3831 (2016).

[2] Y. Ogo, H. Hiramatsu, K. Nomura, H. Yanagi, T. Kamiya, M. Kimura, M. Hirano, and H. Hosono, Phys. Status Solidi A **206**, 2187 (2009).

[3] A. Togo, F. Oba, I. Tanaka, and K. Tatsumi, Phys. Rev. B **74**, 195128 (2006).

[4] K. O. Egbo, C. P. Liu, C. E. Ekuma, and K. M. Yu, J. Appl. Phys. **128**, 135705 (2020).

[5] K. O. Egbo, C. E. Ekuma, C. P. Liu, and K. M. Yu, Phys. Rev. Mater. **4**, 104603 (2020).

[6] K. O. Egbo, M. Kong, C. P. Liu, and K. M. Yu, J. Alloys Compd. **835**, 155269 (2020).

[7] M. Nolan and S. D. Elliott, Phys. Chem. Chem. Phys. **8**, 5350 (2006).

[8] Y. Ogo, H. Hiramatsu, K. Nomura, H. Yanagi, T. Kamiya, M. Hirano, and H. Hosono, Appl. Phys. Lett. **93**, 032113 (2008).

[9] W. Guo, L. Fu, Y. Zhang, K. Zhang, L. Y. Liang, Z. M. Liu, H. T. Cao, and X. Q. Pan, Appl. Phys. Lett. **96**, 042113 (2010).

[10] A. Seko, A. Togo, F. Oba, and I. Tanaka, Phys. Rev. Lett. **100**, 045702 (2008).

[11] J. P. Allen, D. O. Scanlon, S. C. Parker, and G. W. Watson, J. Phys. Chem. C **115**, 19916 (2011).

[12] A. Walsh and G. W. Watson, Phys. Rev. B **70**, 235114 (2004).

[13] D. B. Granato, J. A. Caraveo-Frescas, H. N. Alshareef, and U. Schwingenschlögl, Appl. Phys. Lett. **102**, 212105 (2013).

[14] J. A. Caraveo-Frescas, P. K. Nayak, H. A. Al-Jawhari, D. B. Granato, U. Schwingenschlögl, and H. N. Alshareef, ACS Nano **7**, 5160 (2013).

[15] M. Minohara, A. Samizo, N. Kikuchi, K. K. Bando, Y. Yoshida, and Y. Aiura, J. Phys. Chem. C **124**, 1755 (2020).

[16] S. A. Miller, P. Gorai, U. Aydemir, T. O. Mason, V. Stevanović, E. S. Toberer, and G. J. Snyder, J. Mater. Chem. C **5**, 8854 (2017).

[17] M. Budde, D. Splith, P. Mazzolini, A. Tahraoui, J. Feldl, M. Ramsteiner, H. von Wenckstern, M. Grundmann, and O. Bierwagen, Appl. Phys. Lett. **117**, 252106 (2020).

[18] K. Tetzner, K. Egbo, M. Klupsch, R.-S. Unger, A. Popp, T.-S. Chou, S. B. Anooz, Z. Galazka, A. Trampert, O. Bierwagen, and J. Würfl, Appl. Phys. Lett. **120**, 112110 (2022).

[19] Z. Wang, P. K. Nayak, A. Albar, N. Wei, U. Schwingenschlögl, and H. N. Alshareef, Adv. Mater. Interfaces **2**, 1500374 (2015).

[20] K. J. Saji, Y. P. Venkata Subbaiah, K. Tian, and A. Tiwari, Thin Solid Films **605**, 193 (2016).

[21] A. Parisini, P. Mazzolini, O. Bierwagen, C. Borelli, K. Egbo, A. Sacchi, M. Bosi, L. Seravalli, A. Tahraoui, and R. Fornari, J. Vac. Sci. Technol. A **40**, 042701 (2022).

[22] X. Q. Pan and L. Fu, J. Electroceram. **7**, 35 (2001).

[23] M. Budde, P. Mazzolini, J. Feldl, C. Golz, T. Nagata, S. Ueda, G. Hoffmann, F. Hatami, W. T. Masselink, M. Ramsteiner, and O. Bierwagen, Phys. Rev. Mater. **4**, 124602 (2020).

[24] A. B. Mei, L. Miao, M. J. Wahila, G. Khalsa, Z. Wang, M. Barone, N. J. Schreiber, L. E. Noskin, H. Paik, T. E. Tiwald, Q. Zheng, R. T. Haasch, D. G. Sangiovanni, L. F. J. Piper, and D. G. Schlom, Phys. Rev. Mater. **3**, 105202 (2019).

[25] G. Hoffmann, M. Budde, P. Mazzolini, and O. Bierwagen, APL Mater. **8**, 031110 (2020).

[26] P. Vogt and O. Bierwagen, Appl. Phys. Lett. **106**, 081910 (2015).

[27] F. Werner, J. Appl. Phys. **122**, 135306 (2017).

[28] K. M. Adkison, S.-L. Shang, B. J. Bocklund, D. Klimm, D. G. Schlom, and Z.-K. Liu, APL Mater. **8**, 081110 (2020).

[29] C. W. Bale, E. Bélisle, P. Chartrand, S. A. Decterov, G. Eriksson, A. E. Gheribi, K. Hack, I.-H. Jung, Y.-B. Kang, J. Melançon, A. D. Pelton, S. Petersen, C. Robelin, J. Sangster, P. Spencer, and M.-A. Van Ende, Calphad **55**, 1 (2016).

[30] B. Eifert, M. Becker, C. T. Reindl, M. Giar, L. Zheng, A. Polity, Y. He, C. Heiliger, and P. J. Klar, Phys. Rev. Mater. **1**, 014602 (2017).

[31] F. Wang, X. Zhou, J. Zhou, T.-K. Sham, and Z. Ding, J. Phys. Chem. C **111**, 18839 (2007).

[32] P. A. Stadelmann, *JEMS* (JEMS-SWISS, Chemin Rouge 15 CH-1805 Jongny, n.d.).

[33] O. Bierwagen, T. Ive, C. G. Van de Walle, and J. S. Speck, Appl. Phys. Lett. **93**, 242108 (2008).

[34] K. Egbo, J. Lähnemann, A. Falkenstein, J. Varley, and O. Bierwagen, arXiv:2212.06350 (2022).

[35] H. Hayashi, S. Katayama, R. Huang, K. Kurushima, and I. Tanaka, Phys. Status Solidi RRL **9**, 192 (2015).